Cell type mapping of mild malformations of cortical development with oligodendroglial hyperplasia in epilepsy using single-nucleus multiomics

Isabella C. Galvão[1,2], Manuela Lemoine[1,2], Ludmyla Kandratavicius[2,3], Clarissa L. Yasuda[2,4], Marina K. M. Alvim[2,4], Enrico Ghizoni[2,4], Ingmar Blümcke[5], Fernando Cendes[2,4], Fabio Rogerio[2,3], Iscia Lopes-Cendes[1,2], Diogo F. T. Veiga[1,2,*]

[1]Department of Medical Genetics and Genomic Medicine, School of Medical Sciences, University of Campinas (UNICAMP), Campinas, São Paulo, Brazil
[2]The Brazilian Institute of Neuroscience and Neurotechnology (BRAINN), Campinas, São Paulo, Brazil
[3]Department of Pathology, School of Medical Sciences, University of Campinas (UNICAMP), Campinas, São Paulo, Brazil
[4]Department of Neurology, School of Medical Sciences, University of Campinas (UNICAMP), Campinas, São Paulo, Brazil
[5]Department of Neuropathology, Partner of the European Reference Network (ERN) EpiCARE, Universitätsklinikum Erlangen, Friedrich-Alexander-Universität Erlangen-Nürnberg, Erlangen, Germany
[*]Corresponding author: dfveiga@unicamp.br

ABSTRACT

Objective

Mild malformations of cortical development with oligodendroglial hyperplasia in epilepsy (MOGHE) are brain lesions associated with focal epilepsy and characterized by increased oligodendroglial density, heterotopic neurons, and hypomyelination in the white matter. While previous studies have implicated somatic mutations in the *SLC35A2* gene, the cellular and molecular mechanisms underlying MOGHE pathogenesis remain elusive. To address this gap, this study aimed to systematically characterize the cell type composition and molecular alterations of MOGHE lesions at cellular resolution using single-nucleus multiomics profiling.

Methods

We performed single-nucleus multiomics sequencing to obtain paired gene expression and chromatin accessibility profiles of > 31,000 nuclei from gray matter and white matter regions of MOGHE lesions, and compared the results with publicly available neurotypical control datasets.

Results

The analysis of gray and white matter regions from two MOGHE patients revealed significant cellular composition alterations, including the presence of heterotopic neurons and disease-specific

oligodendrocytes populations within the subcortical white matter. MOGHE-specific oligodendrocytes were characterized by the upregulation of synaptic functions and enhanced neuron communication, denoting a possible role in synaptic support and the mediation of glial-neuron interactions in the disease. On the other hand, MOGHE heterotopic neurons were characterized by the upregulation of genes associated with neuronal migration and the Wnt signaling pathway, suggesting a mechanism underlying their atypical localization.

Significance

This high-resolution cell type mapping of MOGHE lesions in clinical samples unveils neuronal and glial populations affected by the disease, and provides novel insights into the pathophysiological mechanisms of MOGHE.

Keywords

MOGHE; malformations of cortical development; epilepsy; single-nucleus RNA sequencing; single-nucleus ATAC sequencing; gene expression; oligodendrocytes

Key Points

- We provide a multimodal cellular atlas of the human cortical and subcortical regions affected in MOGHE
- MOGHE-associated oligodendrocytes showed upregulation of synaptic functions and enhanced neuron communication
- Neuronal migration and Wnt signaling are upregulated in MOGHE heterotopic neurons

INTRODUCTION

Malformations of cortical development (MCDs) encompass a varied group of disorders that arise due to disruptions in the development of the cerebral cortex. MCDs can affect individuals across all age groups, although symptoms typically begin in early childhood and extend to young adulthood and may include epilepsy, developmental delays, and intellectual impairments[1]. MCDs typically manifest as focal epilepsy and include focal cortical dysplasia (FCD) as well as mild malformations of cortical development with oligodendroglial hyperplasia in epilepsy (MOGHE),

73 a neuropathological entity featuring abnormalities predominantly in the white matter, while
74 maintaining normal cortical lamination[2]. This latter characteristic distinguishes MOGHE from
75 FCD, which is characterized by abnormal cortical architecture associated or not with abnormal cell
76 types[3]. MOGHE was proposed as a distinct pathological entity in 2017[2], and was recently included
77 in the International League Against Epilepsy (ILAE) classification of cortical malformations[4]. The
78 increase in oligodendroglia and the appearance of heterotopic neurons in the white matter, together
79 with the blurring of the gray-white matter junction, are the neuropathological hallmarks of this
80 condition. The affected white matter tissue presents with proliferation of oligodendroglial cells
81 expressing Olig2 and irregular areas of hypomyelination due to reduced myelin protein expression.
82 Clinically, MOGHE manifests as focal epilepsy and treatment might require surgical resection of
83 the affected region. MOGHE lesions occur most often in the frontal lobe and have early seizure
84 onset, typically in young children, but may also occur in the temporal lobe, and symptoms may
85 manifest later even in adulthood[5,6].

86 Genetic investigations have found that MOGHE patients frequently harbor somatic brain variants
87 in the *SLC35A2* gene, which encodes a UDP-galactose transporter[7]. One study reported that 45%
88 (9/20) of MOGHE cases presented truncating or frameshift variants in *SLC35A2*[7], while another
89 screening identified *SLC35A2* variants in 47.1% (16/35) of cases[8]. In agreement, the loss of
90 *Slc35a2* has been shown to recapitulate the MOGHE-like phenotype in conditional knockout
91 mouse models[9–11]. Other genes may also play a role, as demonstrated by a case identified with a
92 variant in the *NPRL2* gene[8]. However, the cellular and molecular mechanisms contributing to
93 MOGHE pathogenesis have not been systematically studied.

94 Single-nucleus RNA sequencing (snRNA-seq) and single-nucleus assay for transposase accessible
95 chromatin sequencing (snATAC-seq) have been applied to dissect the cellular diversity of brain
96 tissues in neurological conditions, enabling the discovery of dysregulated cell states involved in
97 diseases including focal MCDs[12–16]. For instance, we previously applied paired snRNA-seq and
98 snATAC-seq to identify cell populations involved in FCD type II pathology, which allowed us to
99 uncover vulnerable neuronal subtypes and activated microglial states in these cortical
100 malformations[15].

101 In this study, we employed multiomics single-nucleus profiling to systematically analyze the
102 cellular landscapes of both gray matter and subcortical white matter of MOGHE tissues, and
103 compared the results with publicly available control datasets. As a result, we characterized
104 perturbed oligodendroglial and neuronal cell populations associated with the condition. Our
105 findings provide novel insights into the pathophysiological mechanisms of MOGHE.

106

107 **MATERIALS & METHODS**

108 **Clinical samples and neuropathological diagnosis**

109 Fresh brain samples were collected from two patients who underwent surgery for drug-resistant
110 focal epilepsy at the Hospital de Clínicas, University of Campinas. All procedures were approved
111 by the Research Ethics Board of our Institution (CAAE: 12112913.3.0000.5404), and written
112 informed consent was obtained from patients or their legal guardians before surgery.

113

114 Representative surgical specimens were either formalin-fixed and paraffin-embedded (FFPE) or
115 snap-frozen in liquid nitrogen and stored at −80°C. FFPE samples were submitted to routine
116 diagnostics in serial 4 µm-sections stained with hematoxylin and eosin (H&E) and submitted to
117 immunohistochemical reactions. For the latter protocol, the sections were exposed to antibodies
118 against Olig2 (glial marker; dilution 1:250, polyclonal, Millipore Sigma, cat#AB9610, Darmstadt,
119 Germany), and MAP2 (neuronal marker; 1:1,000, clone M13, Thermo Fisher, cat#13-1500,
120 Waltham, MA, USA), overnight at room temperature. Then, a detection solution containing the
121 secondary antibody and peroxidase (AdvanceTMHRP®, Dako, cat#K4068, Glostrup, Denmark;
122 or EnvisionTM Flex+, Dako, cat#K8002, Glostrup, Denmark) was added for 30 min at 37°C. 3,3-
123 diaminobenzidine (DAB) was used as a chromogenic substrate and counterstaining was performed
124 with hematoxylin. Negative controls (without primary antibody) were run concurrently with all
125 immunohistochemical reactions. Digitized images were obtained using a CS2 Aperio ScanScope
126 scanner (Aperio Technologies, Vista, CA, USA).

127

128 Samples were neuropathologically classified as MOGHE according to the latest guidelines of the
129 ILAE[4]. Specifically, the specimens showed an increase in oligodendroglial cells (> 2200 Olig2-

130 positive cells/mm^2) and an excess of heterotopic neurons in the white matter (>30 MAP2-positive
131 neurons/mm^2). No cortical cytoarchitectural changes were observed. After histopathological
132 confirmation of MOGHE, a mirror-frozen section of the tissue used for FFPE analysis was
133 dissected using a surgical scalp in a Petri dish on dry ice, allowing separation of the GM and WM.
134 Subsequently, tissue samples were submitted to molecular analyses as described below.
135

136 **Whole-exome sequencing and somatic mutations**

137 Genomic DNA was extracted from MOGHE-WM tissue using the PureLink Genomic DNA Mini
138 Kit (cat# K182001, Invitrogen) following the recommended protocol. Exome capture libraries
139 were generated using the SureSelect Human All Exon v8 kit (Agilent). Paired-end sequencing was
140 performed at 101 base pairs on each side of the DNA fragment on the Illumina NovaSeq 6000
141 platform. Deep sequencing obtained an average of 489 M reads per sample, with a mean depth
142 exome coverage of 530x.

143 Reads were aligned to the hg38 human reference genome using bwa mem 0.7.17[17]. Bam files were
144 sorted and duplicates were removed using Picard tools v.2.18.2. Indel realignment and base quality
145 score recalibration were performed with GATK[18]. Variants were called using the GATK haplotype
146 caller v4.0.5.1[18] and annotated using SnpEff v.4.3[19]. Somatic mutations including single-
147 nucleotide variants and indels were detected using Mutect2 (GATK v.4.0.5.1) with the 1000
148 Genomes panel of normals as controls.

149

150 **Nuclei isolation and multiome library construction**

151 Nuclei were isolated using the Chromium Nuclei Isolation kit (10X Genomics) according to the
152 manufacturer's protocol (CG000505, revision A), which is compatible with the Single Cell
153 Multiome ATAC + Gene Expression assay. Briefly, frozen tissue samples were dissociated with
154 a pestle in lysis buffer and passed through a nuclei isolation column. The isolated nuclei were then
155 resuspended in a debris removal buffer, followed by washes to clear any remaining debris.
156 Recovered nuclei were stained with Trypan blue and counted with a hemocytometer. Nuclei
157 integrity was evaluated under a microscope at 40X or 60X magnification, and nuclei were

158 considered viable if they were roundish and with an intact membrane. We then performed library
159 construction, which included open chromatin transposition and droplet (GEM) formation using a
160 Chromium Controller (10X Genomics). Libraries were prepared using the Multiome ATAC +
161 Gene Expression kit (10X Genomics) following the manufacturer's protocol (CG000338, Revision
162 E). The quality of the purified ATAC and RNA libraries was assessed using TapeStation (Agilent
163 Technologies).

164

165 **Sequencing and raw data processing**

166 Multiome libraries were sequenced on the Illumina NovaSeq 6000 platform according to the
167 sequencing depth and read length guidelines specified in the Multiome kit protocol (CG000338).
168 Demultiplexing, genome alignment, gene quantification, and peak accessibility analyses for single
169 nuclei were conducted using the Cell Ranger ARC pipeline. Specifically, fastq files were generated
170 with cellranger mkfastq, followed by processing with cellranger-arc count v.2.0.2 using the human
171 genome reference GRCh38 to produce count matrices for RNA and ATAC modalities.
172 Downstream data processing for both snRNA-seq and snATAC-seq were performed using Seurat
173 v.5.0.1[20] and Signac v.1.12.0[21] in R v.4.1.2.

174

175 **snRNA-seq analysis**

176 Ambient RNA decontamination was carried out using DecontX[22] as implemented in the celda[23]
177 v.1.10.0 R package. Briefly, RNA counts for each sample were processed with the decontX
178 function, utilizing the raw droplet matrix generated by cellranger count as background. DecontX
179 then employs a Bayesian approach to estimate and remove contamination in individual cells.
180 Nuclei were filtered using Seurat based on the following criteria: 1000 < UMI counts < 25,000,
181 nFeatures > 400, and mitochondrial read percentage (percent.mt) < 15. Doublet identification was
182 conducted for each sample using scDblFinder[24] v.1.8.0.43.

183 Standard Seurat processing and normalization steps were applied in each sample, including
184 NormalizeData, FindVariableFeatures, ScaleData, RunPCA, RunUMAP, FindNeighbors, and

185 FindClusters. The filtered counts matrix was log-normalized with regression to correct for
186 mitochondrial gene percentage. To correct batch effects across samples, we recomputed
187 NormalizeData, FindVariableFeatures and RunPCA on the merged object, and Harmony[25] v.1.2
188 was used to integrate PCA projections with automatic hyperparameter optimization and default
189 settings. Harmony's algorithm projects cells into a shared space where they cluster based on cell
190 type rather than sample-specific attributes like sequencing batch. Dimensionality reduction was
191 performed using RunUMAP with the first 40 principal components identified using the elbow plot.
192 Clustering was executed with FindNeighbors and FindClusters functions employing the smart
193 local moving (SLM) algorithm, with a resolution set to 1.2.

194 Cell type markers were obtained by applying the Wilcox rank-sum test to RNA-normalized data,
195 with a log2 fold-change threshold of 0.25 and an adjusted P-value of less than 0.05. Differentially
196 expressed genes (DEGs) were identified using MAST. For identifying DEGs in MOGHE-WM vs
197 Control-WM, MAST was applied using the number of counts, mitochondrial percentage and
198 dataset as latent variables. For MOGHE-WM vs MOGHE-GM, we used the number of counts,
199 mitochondrial percentage, donor, and brain region as latent variables. Genes with an adjusted P
200 value of less than 0.05 and fold-change threshold of 2 were considered significant. Mitochondrial
201 genes and those located in sex chromosomes were removed from the analysis.

202 Gene Ontology (GO) and Disease Ontology (DO) enrichment was assessed with clusterProfiler[26]
203 v.4.2.2 and DOSE[27] v.3.20.1 R Packages using the enrichGO and enrichDO functions,
204 respectively. Enrichment analysis with the Synaptic GO (SynGO) ontology[28] to find
205 overrepresented synaptic terms was performed in the SynGO online portal v. 1.2
206 (http://syngoportal.org) using the set of brain expressed genes as the background.

207

208 **Integration with snRNA-seq from heterotypical white matter**

209 We incorporated control white matter snRNA-seq data from two autopsy donors with no
210 neurological history, originally sequenced in Elkjaer et al.[29]. Raw sequencing data were obtained
211 from GEO (accession number GSE231585) and processed with cellranger count v.7.0.1 using the
212 human genome reference GChR38. Nuclei were filtered using Seurat based on the following

criteria: 1000 < UMI counts < 25,000, 200 < nFeatures < 4000, and mitochondrial read percentage (percent.mt) < 1. This dataset was integrated into our MOGHE dataset using the procedure outlined in the "snRNA-seq analysis" section.

snATAC-seq analysis

Samples were preprocessed in Signac to filter out low-quality nuclei based on these criteria: 1,000 < ATAC fragments < 50,000, ATAC fragments in peaks > 400, nucleosome signal < 2, and TSS enrichment > 2. Peaks within each sample were identified using MACS2[30]. Standard processing and normalization were applied with the following functions: RunTFIDF, FindTopFeatures, RunSVD, and FindClusters. The peak counts matrix for each sample was normalized using RunTFIDF to adjust for differences in sequencing depth. Dimensionality reduction was performed with latent semantic indexing (LSI) via the RunSVD function, with UMAP projection utilizing LSI components 2-30, as the first LSI component was determined to represent technical variation. Prior to sample integration, a common peak set across samples was created using MACS2, and peaks in each sample were quantified with the FeatureMatrix function. Peaks located in non-standard chromosomes and blacklisted regions were excluded from subsequent analyses. We then re-computed RunTFIDF, FindTopFeatures, and RunSVD on the merged dataset, and applied Harmony[25] to integrate low-dimensional cell embeddings (LSI components 2-30) across samples, using parameters similar to those defined for RNA analysis. Chromatin accessibility at the gene level was computed with the GeneActivity function from the Signac package, which sums the fragments intersecting the gene body and promoter regions of each gene.

Multimodal data integration

To integrate gene expression and chromatin accessibility data, we utilized Weighted Nearest Neighbor (WNN) analysis, an unsupervised method that evaluates the contribution of each modality and constructs a combined graph representing both RNA and ATAC data. WNN analysis was conducted using the FindMultiModalNeighbors function with 20 neighbors (k.nn), based on UMAP reductions obtained after Harmony[25] integration. The WNN graph was then employed to

241 generate a joint UMAP visualization. Clustering based on the WNN graph was performed using
242 the FindClusters function with the smart local moving (SLM) algorithm. Clusters with fewer than
243 50 nuclei, a high percentage of doublets, or significant enrichment in mitochondrial markers were
244 excluded from further analysis.

245

246 **Cluster annotation**

247 Cell type annotation was performed using Azimuth[20], with the Allen Human Motor Cortex Atlas[31]
248 as the reference dataset. Azimuth performed label transfer by assigning each cell in the MOGHE
249 dataset to the most similar cell type in the reference based on gene expression similarity. The cell
250 type assigned to each cluster was determined by identifying the cell type with the highest mean
251 frequency within that cluster. The Azimuth annotation was manually validated using marker genes,
252 as depicted in Figure 1E. Cluster markers were identified using the FindAllMarkers function on
253 normalized data. Differentially expressed cluster markers were determined with the Wilcox rank-
254 sum test, applying a log2 fold-change threshold of 0.25 and an adjusted P value of less than 0.05.
255 For the oligodendrocyte subcluster analysis, markers were determined using the Wilcox rank-sum
256 test in Seurat with the following parameters: log2 fold-change > 1, percent of cells expressing the
257 marker (pct.1) > 0.3, and adjusted P < 0.05. Mitochondrial genes and those located in sex
258 chromosomes were removed from marker genes.

259

260 **Differential cellular abundance**

261 We utilized the permutation_test function from the scProportionTest R package[32] v. 0.0.0.9 to
262 assess changes in cell type composition between tissue types (MOGHE-WM *vs* Control-WM and
263 MOGHE-WM *vs* MOGHE-GM). The significance test used 10,000 permutations, and cell type
264 changes with a false discovery rate (FDR) less than 0.05 and a fold difference greater than 2 were
265 considered statistically significant.

266

267 **Gene signature analysis**

Gene signature scores were computed using the AddModuleScore function from the Seurat package applied to log-normalized RNA data. Signatures for oligodendrocyte subtypes were obtained from Jakel et al., 2019[33] and Sadick et al., 2022[34].

Motif enrichment analysis

We utilized chromVAR v3.3.2[35] and Signac to perform motif analysis. Nuclei-level motif activity was computed using the RunChromVAR function in Signac with the set of background peaks matched appropriately. Differential activity of motifs was determined using the FindMarkers function, applying a likelihood ratio (LR) test with ATAC fragment counts as a latent variable, a minimum percentage of cells expressing the motif (min.pct) set to 0.05, and an adjusted p-value cutoff of < 0.05. To ensure biologically-relevant results, motifs were further filtered based on the expression of their associated regulators, which were required to be expressed in at least 10% of the cells within a given cluster/cell type.

Cellular communication analysis

Cellular communication was performed using the CellChat R package v.2.1.2[36]. In brief, CellChat utilizes a mass-action-based model to quantify the signaling communication probability between two cell groups using a database of known ligand-receptor interactions. The cellular communication probabilities were computed using the computeCommunProb function with the parameter type set to triMean, and communications between groups with fewer than 10 cells were filtered out. Differential signaling interactions between MOGHE subclusters were calculated by performing differential expression analysis with identifyOverExpressedGenes and netMappingDEG functions, with a percentage of cells expressing the gene > 0.1 and p-value < 0.05. Significant interactions were classified as upregulated for ligands exhibiting a fold-change > 1.5.

RESULTS

299 **Multimodal single-nucleus profiling of MOGHE lesions**

300 We obtained frozen brain specimens from two donors aged 22 and 57 years with a confirmed
301 pathological diagnosis of MOGHE after epilepsy surgery (Table 1). After isolating nuclei from the
302 MOGHE gray matter (MOGHE-GM) and white matter regions (MOGHE-WM), we performed
303 paired snRNA-seq and snATAC-seq on each nucleus using the 10X Genomics Multiome assay to
304 measure chromatin accessibility and gene expression at nuclei resolution (Figure 1A). The
305 sequenced tissues fulfilled the histopathological criteria for MOGHE, presenting with increase of
306 the oligodendrocyte density in the WM and excess of heterotopic neurons (Figure 1B, Methods).
307 Deep exome sequencing of the donors using the MOGHE-WM has not detected somatic variants
308 in *SLC35A2* or in genes previously reported in epileptogenic brain lesions[37].

309 After filtering to remove low-quality nuclei and doublets (Methods), we obtained 31,659 nuclei
310 derived from MOGHE samples in the multiome snATAC-seq + snRNA-seq dataset (Figure 1C).
311 Next, we integrated our MOGHE dataset with snRNA-seq performed on white matter from two
312 neurotypical individuals (Control-WM) obtained from Elkjaer et al.[29], resulting in a total of 39,743
313 nuclei (Figure 1D, Table 1). Clustering analysis identified 33 distinct clusters after integration of
314 MOGHE and control nuclei (Figure S1A). Cell type annotation was carried out using Azimuth[20],
315 and subsequently validated through manual inspection of canonical marker genes (Figure 1E). The
316 Azimuth annotation enabled confident labeling of most of these clusters (Figure S1B), and most
317 clusters were shared across multiple samples (Figure S1C). After annotation, the majority of nuclei
318 was classified as oligodendrocytes (OLs), followed by excitatory neurons (ENs, further divided
319 into upper- and deep-layer subsets), astrocytes, inhibitory neurons (INs, subclassified into Vip,
320 Sst, Pvalb, Lamp5 and Scng subtypes), oligodendrocyte precursor cells (OPCs), microglia and
321 endothelial/vascular and leptomeningeal cells (Endo/VLMCs). As expected, samples derived from
322 white matter (MOGHE-WM and Controls-WM) were predominantly composed of OLs, while
323 neurons were not detected in Controls-WM and primarily located within MOGHE-GM (Figure
324 S1D).

325 We also examined gene accessibility profiles computed based on the chromatin accessibility
326 (snATAC-seq) for the same set of markers (Figure 1F). Gene accessibility displayed a strong
327 correlation with gene expression across cell type markers, with the exception of some endothelial
328 markers, denoting the agreement between data modalities. Thus, our single-nucleus profiling

329 identified the various cortical cell types in GM and subcortical WM regions, revealing the cellular
330 diversity of MOGHE lesions.
331

332 **Cellular and gene expression changes in MOGHE white matter**

333 To investigate disease-associated changes in the WM, we analyzed cell type proportions between
334 MOGHE-WM and Controls-WM as well as MOGHE-WM and MOGHE-GM. Compared to
335 Controls-WM, MOGHE-WM tissue had a higher proportion of ENs, INs and microglia, denoting
336 the expansion of heterotopic neurons and OLs in the WM of the abnormal tissue (Figure 2A). Also,
337 MOGHE-WM had an increased proportion of OLs and a decreased abundance of astrocytes, ENs,
338 and INs compared to MOGHE-GM, reflecting the expected differences in cell composition
339 between cortical and subcortical regions (Figure 2B).

340 We also analyzed differentially expressed genes (DEGs) between tissue conditions and within each
341 cell type. Neurons were not considered in this analysis since they were not identified in Controls-
342 WM. In MOGHE-WM compared to Controls-WM, there were significant gene expression changes
343 in most glial populations, including astrocytes, microglia, and OLs (Figure 2C). When compared
344 to MOGHE-GM, OLs in MOGHE-WM were the most affected population with a large number of
345 downregulated genes (Figure 2C). Collectively, these analyses indicate that the cellular
346 composition of subcortical MOGHE-WM was characterized by an increased OL population and
347 the presence of heterotopic neurons, which recapitulated key hallmarks of the disease. Meanwhile,
348 gene expression changes revealed that nearly all glial cell types in subcortical MOGHE-WM were
349 affected by the condition.

350

351 **Pathological oligodendrocyte states in MOGHE**

352 To identify MOGHE-associated OLs, we performed a subclustering analysis in the OLs
353 compartment and assessed whether these subpopulations were enriched in disease tissue. Notably,
354 subclusters 4 and 7 (OL_4 and OL_7), which clustered separately from the major OLs population,
355 were predominantly observed in MOGHE (Figure 3A). Differential cellular abundance analysis
356 confirmed that OL_4 and OL_7 were significantly expanded in MOGHE-WM compared to

357 Controls-WM (Figure 3B, top). We inspected the subcluster distribution in individual samples and
358 according to their localization (Figures S2A,B). The OL_4 subcluster was detected in both
359 sequenced MOGHE samples and derived from WM and GM regions (n = 2,344 cells, 48%
360 MOGHE-WM, 52% MOGHE-GM). The OL_7 subcluster was detected mostly in the WM of the
361 G23 sample (n = 1,201 cells, 97% MOGHE-WM, 3% MOGHE-GM). Thus, this analysis
362 uncovered disease-specific OLs subpopulations emerging in the cortical and subcortical regions
363 of MOGHE lesions.

364 Next, we used two approaches to functionally annotate these MOGHE-associated OLs. First, we
365 performed differential marker analysis followed by enrichment analysis to identify subcluster-
366 enriched biological themes. This approach revealed subcluster-specific marker genes for OL_4 (n
367 = 220, adj. $P < 0.05$) and OL_7 subclusters (n = 967, adj. $P < 0.05$) (Supplemental Table 1, top 50
368 markers shown in Fig. 3C). OL_4 marker genes were strongly associated with synapse-related
369 functions such as modulation of chemical synaptic transmission (adj. $P = 6.6 \times 10^{-19}$), regulation
370 of trans-synaptic signaling (adj. $P = 6.6 \times 10^{-19}$), regulation of membrane potential (adj. $P = 1.6 \times$
371 10^{-15}), synaptic organization (adj. $P = 4.9 \times 10^{-14}$) and synapse assembly (adj. $P = 4.7 \times 10^{-10}$)
372 (Figure 3D, Supplemental Table 1). Notably, these synaptic functions were also overrepresented
373 among OL_7 markers, however they were not enriched in other OLs subclusters (Figure 3D). For
374 instance, top expressed OL_4 markers included synaptic-related genes *APOE4*, *MEF2C*, *LFRN5*,
375 *PLCB1*, *ADGLR2* (Figure 3C). On the other hand, top OL_7 markers included synaptic-related
376 genes *C3*, *SYT7*, *CUX2* and *CACNA1A* (Figure 3C).

377 Based on these observations, we used the Synaptic Gene Ontology (SynGO), a comprehensive
378 resource containing curated annotation of synaptic genes, to further investigate the functions
379 associated with OL_4 and OL_7 subsets. In the OL_4 subcluster, we found that 28 genes (out of
380 top 50 markers) were linked to synaptic components ($q = 6.8 \times 10^{-18}$, Figure S2C, Supplemental
381 Table 2), of which 17 were postsynaptic genes ($q = 2 \times 10^{-10}$) and 15 presynaptic genes ($q = 4.1 \times$
382 10^{-10}). Similarly, we observed significant enrichment for synaptic genes in OL_7 (n = 13, $q = 1.5$
383 $\times 10^{-4}$), especially posynaptic genes (n=10, $q = 1.7 \times 10^{-4}$) (Figure S2C, Supplemental Table 2).
384 Of note, functional enrichment using the Disease Ontology showed that MOGHE-specific OL_4
385 and OL7 were the only subclusters enriched for genes related to epilepsy and brain diseases (Figure
386 3E, Supplemental Table 1). For instance, OL_4 and OL_7 expressed markers linked to epilepsy[38]

387 such as *SLC1A2*, *KNCQ2*, *KCNQ3* (Figure 3H). Collectively, these analyses showed that
388 MOGHE-specific OLs upregulated synaptic components and epilepsy-related genes.

389 The other approach to characterize MOGHE OLs involved comparison with gene signatures from
390 pathological OLs in the literature. Previous snRNA-seq studies described the OLs subset known
391 as the immune subtype (ImOLGs) and the integrated 2 subtype (Int2), which were identified in
392 multiple sclerosis and Alzheimer's disease, respectively[33,34]. We used the AddModuleScore from
393 Seurat to score these pathological signatures in OLs identified in MOGHE lesions. Notably, OL_4
394 and OL_7 exhibited the highest scores for ImOLGs (Figure 3F) and Int2 (Figure 3G) signatures,
395 indicating that MOGHE-specific OL_4 and OL_7 shared marker genes with these OLs subtypes
396 identified in other neurological diseases. Common markers with the ImOLGs subtype included
397 *MEF2C* and *APOE* (expressed in OL_4), and immune genes *CD74*, *DOCK8*, *APBB1IP* and *C3*,
398 which are highly expressed in OL_7 (Figure 3H).

399 In addition, *OLIG2*, which encodes the protein considered to be a neuropathological marker of the
400 expanded oligodendroglia cell clusters in MOGHE[2,7,39], was expressed only in the MOGHE-
401 specific OL_7 subpopulation (Figure S2E), even though the chromatin in *OLIG2* promoter region
402 was accessible across all OL subclusters (Figure S2F). On the other hand, *OLIG2* was not detected
403 in MOGHE-specific OL_4, thus indicating that other markers need to be considered for detecting
404 pathological OLs in the tissue.

405 Altogether, these in-depth analyses of the OL compartment enabled us to identify MOGHE-
406 specific OLs cell states associated with synapse regulation and sharing common markers with
407 pathological OLs from other neurological conditions.

408 **Cellular communication of MOGHE oligondendrocytes**

409 We inferred the cell communication network among the identified OLs subclusters and other cell
410 types using CellChat[40]. First, we analyzed the global communication patterns by considering major
411 cell types and including OL subclusters (Figure 4A). Neurons exhibited the most robust
412 communication patterns, particularly with other neurons. Notably, among the OL subclusters,
413 OL_4 and OL_7 showed the highest communication strength, especially with neurons and OPCs.

414 Next, we conducted a differential analysis using CellChat to identify specific signaling interactions
415 in OL_4 and OL_7 compared to other OL subclusters. This analysis revealed 12 and 63
416 significantly upregulated ligand-receptor pairs in OL_4 and OL_7, respectively. Examples of
417 upregulated interactions in OL_4 (Figures 4B,D) included neuronal growth factor signaling
418 (NEGR1 (OL) → NEGR1 (OL/Neuron)), neurexin signaling (NRXN1 (OL) → CLSTN2 (Neuron)
419 and NRXN1 (OL) → LRRTM3 (OPC)), and neuroligin signaling (LRRC4C (OL) → NTNG1
420 (OPC)). In OL 7 (Figures 4C,D), the upregulated pathways involved PTPR signaling (PTPRS (OL)
421 → LRNF5 (OL) and PTPRS (OL) → LRRTM4 (Neuron/OPC)), neurexin signaling (NRXN1 (OL)
422 → NGLN3 (OL) and NRXN1 (OL) → CLSTN2 (Neuron)), and neuregulin signaling (NRG1 (OL)
423 → ERBB3 (OPC/OL)). In line with previous GO analyses, these interactions within the neurexin,
424 neuroligin and neuregulin signaling pathways are implicated in synaptic organization[41,42] and
425 oligodendrocyte differentiation[43,44]. These results highlight the distinct communication patterns of
426 MOGHE-specific OL_4 and OL_7 subclusters particularly through interactions with neurons and
427 OPCs, suggesting their functional specialization in synaptic regulation.

428 **Characterization of heterotopic neurons in MOGHE**

429 Next, given that the appearance of heterotopic neurons (HNs) is a key histological feature of
430 MOGHE, we asked whether misplaced neurons could be identified in the WM of MOGHE
431 samples. We identified a subpopulation of HNs derived specifically from MOGHE-WM in both
432 patients (n = 246; Figures 5A,B), while HNs were not detected in Control-WM samples. Most of
433 these HNs were annotated as ENs from layers 5/6 (n = 129; 52%), and the remaining nuclei
434 consisted mainly of INs subtypes Lamp5, Sst and PvalB. The HNs subpopulation expressed a very
435 distinct set of markers such as cell-adhesion genes (*CDH5* and *CDH3*), transmembrane proteins
436 (*TMEM275* and *TMEM233*), ion channels (*KCNK2*, *CACNA1B*), and the neurotransmitter *NPY*
437 (Figure 5C, Supplemental Table 3).
438 To identify molecular functions in this abnormal neuronal subpopulation, we analyzed DEGs
439 between HNs (i.e. MOGHE-WM neurons) and total MOGHE-GM neurons, identifying 255
440 upregulated and 233 downregulated genes (Figure 5D, Supplemental Table 3). Enriched GO terms
441 associated with downregulated genes included negative regulation of neuron projection,
442 cytoplasmic translation, and cell junction assembly (Figure 5E). On the other hand, upregulated
443 molecular functions included positive regulation of cell projection, the Fc receptor-mediated

444 stimulatory signaling pathway, and the Wnt signaling pathway (Figure 5F), which has been shown
445 to regulate neuronal migration[45,46].
446 In line with the DEG analysis, a motif enrichment analysis based on the snATAC-seq data
447 identified that FOX transcriptional regulators were among the top activated motifs in HNs (Figure
448 5F). The FOX family has been shown to regulate the Wnt signaling pathway[47,48], which could
449 explain the distinctive Wnt activation in HNs. Therefore, these results indicate that HNs in
450 MOGHE consisted of ENs from deep cortical layers with increased expression of pathways
451 associated with neuronal migration.
452

453 **DISCUSSION**

454 In this study, we applied multiomic single-nucleus profiling to systematically map the cellular
455 landscapes of cortical and subcortical regions affected in MOGHE, a type of focal MCD
456 characterized by white matter abnormalities and associated with epilepsy. We identified significant
457 alterations in cell type composition in the WM of MOGHE tissues and uncovered distinct
458 pathological cell populations in this condition.

459 We identified disease-specific OLs subpopulations emerging in MOGHE tissue with unique
460 transcriptomic profiles. Gene ontology and cell-to-cell communication analyses revealed
461 functional differences between MOGHE-specific OLs subclusters and the remaining
462 oligodendrocytes, notably the upregulation of synaptic genes and enhanced neuron
463 communication. Thus, we postulate that MOGHE-specific OLs may be involved in synaptic
464 support and the mediation of glial-neuron interactions in the disease.

465 OPCs are the specific glial cells that directly form synapses with neurons[49]. Yet, oligodendroglia
466 are a transcriptionally heterogeneous lineage with distinct populations emerging in response to
467 neurological conditions[50,33,51]. For example, snRNA-seq in human OLs from WM controls and
468 multiple sclerosis found that OPCs and committed oligodendrocytes precursors (COPs) were
469 enriched in synapse regulation[33]. Sadick et al also identified OLs populations enriched for
470 transcripts involved in synapse assembly and organization in Alzheimer's disease[51]. Thus, the
471 emergence of synapse-enriched OLs in neurological conditions associated with WM degradation

472 and myelin loss[49,52] such as multiple sclerosis and Alzheimer's has been described, however the
473 roles of these synapse-enriched OLs remain unknown.

474 Some of the markers associated with MOGHE OLs have established functions. For example,
475 *APOE4*, a marker of the OL_4 subpopulation, has been shown to impair oligodendrocyte
476 differentiation[53] and downregulate myelination via cholesterol dysregulation[54]. Cholesterol
477 biosynthesis is essential for myelin biogenesis[55,56]. Thus, these dysregulated OLs states might
478 contribute to WM matter degradation and the formation of irregular zones of hypomyelination
479 typically observed in MOGHE-WM. On the other hand, the OL_7 subcluster expressed markers
480 of immune cells such as *C3*, *CD74*, and *CD83*, therefore sharing a common transcription profile
481 with the immune oligodendroglia (ImOLG) population described in multiple sclerosis[33].

482 Other glial cell types may also contribute to the disease, as evidenced by microglia increase in
483 MOGHE-WM. Microglia have been linked to epilepsy and their effects can be pro- or anti-
484 inflammatory depending on the disease stage[57,58]. Moreover, resident microglia are required for
485 maintaining myelin health and their dysregulation may be related to the emergence of pathological
486 OL states[59].
487
488 We also identified the appearance of misplaced neurons in the WM (HNs), another key
489 pathological hallmark of MOGHE. Even though MOGHE HNs were a rare population, we could
490 identify specific biological functions in this neuronal subset. We found that MOGHE HNs
491 displayed increased expression of neuronal projection genes and Wnt signaling pathway.
492 Interestingly, Wnt signaling has been linked to axonal/dendrite remodeling and neuronal
493 plasticity[60,61], and regulates neuronal migration by modulating the microtubule cytoskeleton[45,46],
494 providing a potential mechanism for the abnormal localization of HNs. Furthermore, alterations in
495 Wnt signaling induce neuronal hyperexcitability[62,63], a defining feature of epilepsy. Thus,
496 MOGHE HNs represent a disease-specific neuronal population that may contribute to the
497 development of epileptogenic circuits in MOGHE.
498
499 While our findings provide valuable insights into the cellular landscape of MOGHE, this study has
500 limitations due to its restricted sample size. For instance, while the MOGHE-specific OL_4
501 subcluster was observed in both patients, OL_7 was predominantly derived from a single patient.

Future studies with larger cohorts are warranted to confirm the MOGHE-associated OL subpopulations identified here and may reveal additional cellular states linked to the disease. Furthermore, our results indicated that some MOGHE-specific OLs derived from the OL_4 subcluster were located in the GM, possibly due to the blurring of the gray-white matter junction in lesions. Spatial transcriptomics and/or in situ immunohistochemistry studies using the markers identified in this study will be needed to determine the localization of MOGHE-specific OLs in lesions. In addition, incorporating cases with *SLC35A2* loss-of-function variants will be important for understanding the impact of this common genetic variation on the cellular heterogeneity of the disease.

In summary, this high-resolution mapping of MOGHE lesions in clinical samples represents the first cellular atlas of human tissue affected by the disease, providing a comprehensive view of the perturbed cell populations and gene expression alterations involved in this pathology.

Data Availability

Raw and processed sequencing datasets from paired snRNA-seq and snATAC-seq generated in this study were deposited at the Gene Expression Omnibus under accession code GSE284073.

Author contributions

D.F.T.V. and F.R. designed the study. M.L. performed single-nucleus assays. I.C.G. and D.F.T.V. performed data analyses. C.L.Y., E.G., H.T., M.K.M.A., F.C., and I.L-C contributed to clinical sample collection. L.K., I.B. and F.R. performed histopathological analyses. I.C.G. and D.F.T.V. wrote the manuscript. All authors reviewed and approved the final version of the manuscript.

Funding Sources

This work was supported by Fundação de Amparo à Pesquisa do Estado de São Paulo (FAPESP) [grant numbers 2019/07382-2, 2022/01530-2, 2019/08259-0, 2013/07559-3]; the Chan Zuckerberg Initiative DAF, an advised fund of the Silicon Valley Community Foundation [grant number DAF2021-237598]; Conselho Nacional de Pesquisa (CNPq) [grant number 311923/2019-4]; Coordenação de Aperfeiçoamento de Pessoal de Nível Superior (CAPES).

533 **Declaration of interests**

534 None of the authors has any conflict of interest to disclose.

535

536 **Ethics approval and patient consent**

537 We confirm that we have read the Journal's position on issues involved in ethical publication and
538 affirm that this report is consistent with those guidelines. This study was approved by the
539 University of Campinas' Research Ethics Committee (CAAE: 12112913.3.0000.5404), and
540 written informed consent was obtained from patients or their legal guardians.

REFERENCES

1. Severino M, Geraldo AF, Utz N, Tortora D, Pogledic I, Klonowski W, et al. Definitions and classification of malformations of cortical development: practical guidelines. Brain. 2020; 143(10):2874–94.

2. Schurr J, Coras R, Rössler K, Pieper T, Kudernatsch M, Holthausen H, et al. Mild Malformation of Cortical Development with Oligodendroglial Hyperplasia in Frontal Lobe Epilepsy: A New Clinico-Pathological Entity. Brain Pathology. 2017; 27(1):26–35.

3. Blümcke I. Neuropathology and epilepsy surgery: 2022 update. Vol. 3, Free Neuropathology. University of Muenster; 2022.

4. Najm I, Lal D, Alonso Vanegas M, Cendes F, Lopes-Cendes I, Palmini A, et al. The ILAE consensus classification of focal cortical dysplasia: An update proposed by an ad hoc task force of the ILAE diagnostic methods commission. Epilepsia. 2022; 63(8):1899–919.

5. Mendes Coelho VC, Morita-Sherman M, Yasuda CL, Alvim MMK, Amorim BJ, Tedeschi H, et al. Magnetic resonance imaging findings and clinical characteristics in mild malformation of cortical development with oligodendroglial hyperplasia and epilepsy in a predominantly adult cohort. Epilepsia. 2021; 62(6):1429–41.

6. Gaballa A, Woermann FG, Cloppenborg T, Kalbhenn T, Blümcke I, Bien CG, et al. Clinical characteristics and postoperative seizure outcome in patients with mild malformation of cortical development and oligodendroglial hyperplasia. Epilepsia. 2021; 62(12):2920–31.

7. Bonduelle T, Hartlieb T, Baldassari S, Sim NS, Kim SH, Kang H-C, et al. Frequent SLC35A2 brain mosaicism in mild malformation of cortical development with oligodendroglial hyperplasia in epilepsy (MOGHE). Acta Neuropathologica Communications. 2021; 9(1):3.

8. López-Rivera JA, Leu C, Macnee M, Khoury J, Hoffmann L, Coras R, et al. The genomic landscape across 474 surgically accessible epileptogenic human brain lesions. Brain. 2022; 146(4):1342.

9. Elziny S, Sran S, Yoon H, Corrigan RR, Page J, Ringland A, et al. Loss of *Slc35a2* alters development of the mouse cerebral cortex. Neuroscience Letters. 2024; 836:137881.

10. Spyrou J, Aung KP, Vanyai H, Leventer RJ, Maljevic S, Lockhart PJ, et al. *Slc35a2* mosaic knockout impacts cortical development, dendritic arborisation, and neuronal firing. Neurobiology of Disease. 2024; 201:106657.

11. Yoon H, Ringland A, Anderson JJ, Sran S, Elziny S, Huynh C, et al. Mouse models of Slc35a2 brain mosaicism reveal mechanisms of mild malformations of cortical development with oligodendroglial hyperplasia in epilepsy. Epilepsia. 2024; .

575 12. Liddelow SA, Guttenplan KA, Clarke LE, Bennett FC, Bohlen CJ, Schirmer L, et al.
576 Neurotoxic reactive astrocytes are induced by activated microglia. Nature. 2017;
577 541(7638):481–7.

578 13. Olah M, Menon V, Habib N, Taga MF, Ma Y, Yung CJ, et al. Single cell RNA sequencing
579 of human microglia uncovers a subset associated with Alzheimer's disease. Nat Commun.
580 2020; 11(1):6129.

581 14. Adams L, Song MK, Yuen S, Tanaka Y, Kim Y-S. A single-nuclei paired multiomic
582 analysis of the human midbrain reveals age- and Parkinson's disease–associated glial
583 changes. Nature aging. 2024; 4(3):364.

584 15. Galvão IC, Lemoine M, Messias LA, Araújo PAORA, Geraldis JC, Yasuda CL, et al.
585 Multimodal single-cell profiling reveals neuronal vulnerability and pathological cell states
586 in focal cortical dysplasia. iScience [Internet]. 2024 [cited 2024]; 27(12). Available from:
587 https://www.cell.com/iscience/abstract/S2589-0042(24)02562-8

588 16. Walter TJ, Suter RK, Ayad NG. An overview of human single-cell RNA sequencing studies
589 in neurobiological disease. Neurobiology of Disease. 2023; 184:106201.

590 17. Li H, Durbin R. Fast and accurate short read alignment with Burrows–Wheeler transform.
591 Bioinformatics. 2009; 25(14):1754–60.

592 18. DePristo MA, Banks E, Poplin RE, Garimella KV, Maguire JR, Hartl C, et al. A framework
593 for variation discovery and genotyping using next-generation DNA sequencing data. Nat
594 Genet. 2011; 43(5):491–8.

595 19. Cingolani P, Platts A, Wang LL, Coon M, Nguyen T, Wang L, et al. A program for
596 annotating and predicting the effects of single nucleotide polymorphisms, SnpEff. Fly
597 (Austin). 2012; 6(2):80–92.

598 20. Hao Y, Hao S, Andersen-Nissen E, Mauck WM, Zheng S, Butler A, et al. Integrated
599 analysis of multimodal single-cell data. Cell. 2021; 184(13):3573-3587.e29.

600 21. Stuart T, Srivastava A, Madad S, Lareau CA, Satija R. Single-cell chromatin state analysis
601 with Signac. Nat Methods. 2021; 18(11):1333–41.

602 22. Yang S, Corbett SE, Koga Y, Wang Z, Johnson WE, Yajima M, et al. Decontamination of
603 ambient RNA in single-cell RNA-seq with DecontX. Genome Biology. 2020; 21(1):57.

604 23. celda [Internet]. Bioconductor. [cited 2024]. Available from:
605 http://bioconductor.org/packages/celda/

606 24. Germain P-L, Lun A, Garcia Meixide C, Macnair W, Robinson MD. Doublet identification
607 in single-cell sequencing data using scDblFinder. F1000Res. 2021; 10:979.

608 25. Korsunsky I, Millard N, Fan J, Slowikowski K, Zhang F, Wei K, et al. Fast, sensitive and
609 accurate integration of single-cell data with Harmony. Nat Methods. 2019; 16(12):1289–96.

610 26. Wu T, Hu E, Xu S, Chen M, Guo P, Dai Z, et al. clusterProfiler 4.0: A universal enrichment
611 tool for interpreting omics data. Innovation [Internet]. 2021 [cited 2024]; 2(3). Available
612 from: https://www.cell.com/the-innovation/abstract/S2666-6758(21)00066-7

613 27. Yu G, Wang L-G, Yan G-R, He Q-Y. DOSE: an R/Bioconductor package for disease
614 ontology semantic and enrichment analysis. Bioinformatics. 2015; 31(4):608–9.

615 28. Koopmans F, Nierop P van, Andres-Alonso M, Byrnes A, Cijsouw T, Coba MP, et al.
616 SynGO: An Evidence-Based, Expert-Curated Knowledge Base for the Synapse. Neuron.
617 2019; 103(2):217-234.e4.

618 29. Elkjaer ML, Hartebrodt A, Oubounyt M, Weber A, Vitved L, Reynolds R, et al. Single-Cell
619 Multi-Omics Map of Cell Type–Specific Mechanistic Drivers of Multiple Sclerosis
620 Lesions. Neurology Neuroimmunology & Neuroinflammation. 2024; 11(3):e200213.

621 30. Zhang Y, Liu T, Meyer CA, Eeckhoute J, Johnson DS, Bernstein BE, et al. Model-based
622 Analysis of ChIP-Seq (MACS). Genome Biology. 2008; 9(9):R137.

623 31. Bakken TE, Jorstad NL, Hu Q, Lake BB, Tian W, Kalmbach BE, et al. Comparative
624 cellular analysis of motor cortex in human, marmoset and mouse. Nature. 2021;
625 598(7879):111–9.

626 32. Miller SA, Policastro RA, Sriramkumar S, Lai T, Huntington TD, Ladaika CA, et al. LSD1
627 and Aberrant DNA Methylation Mediate Persistence of Enteroendocrine Progenitors That
628 Support BRAF-Mutant Colorectal Cancer. Cancer Res. 2021; 81(14):3791–805.

629 33. Jäkel S, Agirre E, Mendanha Falcão A, van Bruggen D, Lee KW, Knuesel I, et al. Altered
630 human oligodendrocyte heterogeneity in multiple sclerosis. Nature. 2019; 566(7745):543–
631 7.

632 34. Sadick JS, O'Dea MR, Hasel P, Dykstra T, Faustin A, Liddelow SA. Astrocytes and
633 oligodendrocytes undergo subtype-specific transcriptional changes in Alzheimer's disease.
634 Neuron. 2022; 110(11):1788-1805.e10.

635 35. Schep AN, Wu B, Buenrostro JD, Greenleaf WJ. chromVAR: inferring transcription-factor-
636 associated accessibility from single-cell epigenomic data. Nature Methods. 2017;
637 14(10):975–8.

638 36. Jin S, Plikus MV, Nie Q. CellChat for systematic analysis of cell–cell communication from
639 single-cell transcriptomics. Nat Protoc. 2025; 20(1):180–219.

640 37. López-Rivera JA, Leu C, Macnee M, Khoury J, Hoffmann L, Coras R, et al. The genomic
641 landscape across 474 surgically accessible epileptogenic human brain lesions. Brain. 2023;
642 146(4):1342–56.

643 38. Macnee M, Pérez-Palma E, López-Rivera JA, Ivaniuk A, May P, Møller RS, et al. Data-
644 driven historical characterization of epilepsy-associated genes. European Journal of
645 Paediatric Neurology. 2023; 42:82–7.

646 39. Blümcke I. Neuropathology and epilepsy surgery: 2022 update. Free Neuropathol. 2022;
647 3:3–12.

648 40. Jin S, Plikus MV, Nie Q. CellChat for systematic analysis of cell–cell communication from
649 single-cell transcriptomics. Nat Protoc. 2025; 20(1):180–219.

650 41. Cuttler K, Hassan M, Carr J, Cloete R, Bardien S. Emerging evidence implicating a role for
651 neurexins in neurodegenerative and neuropsychiatric disorders. Open Biol. 2021;
652 11(10):210091.

653 42. Tagliaferro M, Ponti D. The Signaling of Neuregulin-Epidermal Growth Factor Receptors
654 and Its Impact on the Nervous System. Neuroglia. 2023; 4(4):253–74.

655 43. Proctor DT, Stotz SC, Scott LOM, de la Hoz CLR, Poon KWC, Stys PK, et al. Axo-glial
656 communication through neurexin-neuroligin signaling regulates myelination and
657 oligodendrocyte differentiation. Glia. 2015; 63(11):2023–39.

658 44. Liu X, Hua F, Yang D, Lin Y, Zhang L, Ying J, et al. Roles of neuroligins in central
659 nervous system development: focus on glial neuroligins and neuron neuroligins. J Transl
660 Med. 2022; 20(1):418.

661 45. Hayat R, Manzoor M, Hussain A. Wnt signaling pathway: A comprehensive review. Cell
662 Biology International. 2022; 46(6):863–77.

663 46. Salinas PC. Modulation of the microtubule cytoskeleton: a role for a divergent canonical
664 Wnt pathway. Trends in Cell Biology. 2007; 17(7):333–42.

665 47. den Hoed J, Devaraju K, Fisher SE. Molecular networks of the FOXP2 transcription factor
666 in the brain. EMBO reports. 2021; 22(8):e52803.

667 48. Moparthi L, Koch S. FOX transcription factors are common regulators of Wnt/β-catenin–
668 dependent gene transcription. Journal of Biological Chemistry [Internet]. 2023 [cited 2024];
669 299(5). Available from: https://www.jbc.org/article/S0021-9258(23)00309-5/abstract

670 49. Nasrabady SE, Rizvi B, Goldman JE, Brickman AM. White matter changes in Alzheimer's
671 disease: a focus on myelin and oligodendrocytes. Acta Neuropathologica Communications.
672 2018; 6(1):22.

673 50. Marques S, Zeisel A, Codeluppi S, van Bruggen D, Mendanha Falcão A, Xiao L, et al.
674 Oligodendrocyte heterogeneity in the mouse juvenile and adult central nervous system.
675 Science. 2016; 352(6291):1326–9.

676 51. Sadick JS, O'Dea MR, Hasel P, Dykstra T, Faustin A, Liddelow SA. Astrocytes and
677 oligodendrocytes undergo subtype-specific transcriptional changes in Alzheimer's disease.
678 Neuron. 2022; 110(11):1788-1805.e10.

679 52. Ontaneda D, Hyland M, Cohen JA. Multiple Sclerosis: New Insights in Pathogenesis and
680 Novel Therapeutics. Annual Review of Medicine. 2012; 63(Volume 63, 2012):389–404.

681 53. Mok KK-S, Yeung SH-S, Cheng GW-Y, Ma IW-T, Lee RH-S, Herrup K, et al.
682 Apolipoprotein E ε4 disrupts oligodendrocyte differentiation by interfering with astrocyte-
683 derived lipid transport. J Neurochem. 2023; 165(1):55–75.

684 54. Blanchard JW, Akay LA, Davila-Velderrain J, von Maydell D, Mathys H, Davidson SM, et
685 al. APOE4 impairs myelination via cholesterol dysregulation in oligodendrocytes. Nature.
686 2022; 611(7937):769–79.

687 55. Berghoff SA, Gerndt N, Winchenbach J, Stumpf SK, Hosang L, Odoardi F, et al. Dietary
688 cholesterol promotes repair of demyelinated lesions in the adult brain. Nat Commun. 2017;
689 8(1):14241.

690 56. Saher G, Brügger B, Lappe-Siefke C, Möbius W, Tozawa R, Wehr MC, et al. High
691 cholesterol level is essential for myelin membrane growth. Nat Neurosci. 2005; 8(4):468–
692 75.

693 57. Yu C, Deng X, Xu D. Microglia in epilepsy. Neurobiology of Disease. 2023; 185:106249.

694 58. Olah M, Menon V, Habib N, Taga MF, Ma Y, Yung CJ, et al. Single cell RNA sequencing
695 of human microglia uncovers a subset associated with Alzheimer's disease. Nat Commun.
696 2020; 11(1):6129.

697 59. McNamara NB, Munro DAD, Bestard-Cuche N, Uyeda A, Bogie JFJ, Hoffmann A, et al.
698 Microglia regulate central nervous system myelin growth and integrity. Nature. 2023;
699 613(7942):120–9.

700 60. He C-W, Liao C-P, Pan C-L. Wnt signalling in the development of axon, dendrites and
701 synapses. Open Biology. 2018; 8(10):180116.

702 61. McLeod F, Salinas PC. Wnt proteins as modulators of synaptic plasticity. Current Opinion
703 in Neurobiology. 2018; 53:90–5.

704 62. Jaworski T. Control of neuronal excitability by GSK-3beta: Epilepsy and beyond.
705 Biochimica et Biophysica Acta (BBA) - Molecular Cell Research. 2020; 1867(9):118745.

706 63. Priya, Yadav N, Anand S, Banerjee J, Tripathi M, Chandra PS, et al. The multifaceted role
707 of Wnt canonical signalling in neurogenesis, neuroinflammation, and hyperexcitability in
708 mesial temporal lobe epilepsy. Neuropharmacology. 2024; 251:109942.

709 64. Pandey S, Shen K, Lee S-H, Shen Y-AA, Wang Y, Otero-García M, et al. Disease-
710 associated oligodendrocyte responses across neurodegenerative diseases. Cell Reports.
711 2022; 40(8):111189.

712

713

714 **TABLES WITH TITLES AND LEGENDS**
715

716 **Table 1** - Description of the clinical samples.

Condition	Specimen identifier	Donor	Dissection	Sex	Age at surgery (y)	Age at onset (y)	Lobe	Side of resection	Tissue source	Sequenced nuclei
MOGHE (This study)	G23_GM	G23	GM	F	22	11	Frontal	Right	Epilepsy surgery	4,603
	G23_WM	G23	WM	F	22	11	Frontal	Right	Epilepsy surgery	10,804
	G39_GM	G39	GM	M	57	36	Temporal	Left	Epilepsy surgery	1,593
	G23_WM	G39	WM	M	57	36	Temporal	Left	Epilepsy surgery	14,659
Controls (Elkjaer *et al.*, 2024)	C3	C3	WM	M	68	NA	NA	NA	Post-mortem	3,810
	C4	C4	WM	F	50	NA	NA	NA	Post-mortem	4,274

717

718 Abbreviations: F, female; M, male; NA, not available.
719
720
721
722

723 **FIGURES**

724

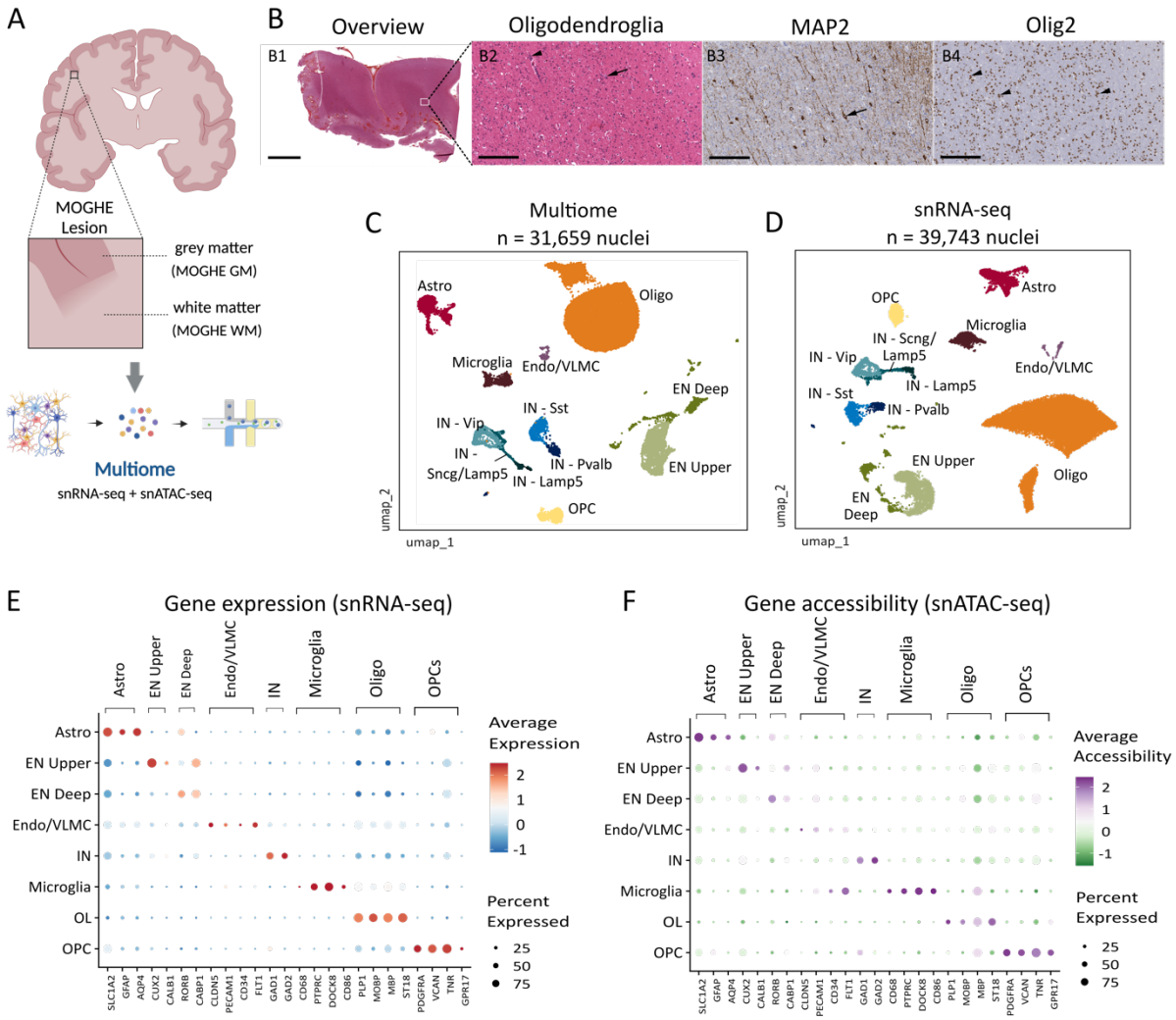

725

726

727 **Figure 1. Multimodal single-nucleus sequencing of MOGHE tissue.**

728 **(A)** Schematic of MOGHE samples and study design. Nuclei from the MOGHE grey matter
729 (MOGHE-GM) and white matter regions (MOGHE-WM) isolated and profiled by snRNA-seq
730 and snATAC-seq using the Multiome assay (10X Genomics). Created with Biorender.

731 **(B)** Representative histopathological findings of a brain surgical sample with MOGHE sequenced
732 in the study. **B1.** Hematoxylin and eosin (H&E) stained section showing an overview of the
733 resected tissue. The white rectangle indicates a subcortical WM region near the GM-WM junction
734 presented in B2-B4. **B2.** Clusters of oligodendroglial cells either perivascular (arrow head) or

735 around heterotopic neurons (arrow). **B3.** Immunohistochemistry (IHC) for MAP2 (neurons)
736 depicts scattered heterotopic neurons (arrow). **B4.** IHC for Olig2 (oligodendrocytes) showing an
737 irregularly distributed increase of the oligodendroglial cells, either isolated or in clusters (arrow
738 heads). Scale bars: 4 mm (Figure B1) and 200 µm (Figures B2-B4).
739 **(C)** Joint uniform manifold approximation and projection (UMAP) visualization of snATAC-seq
740 and snRNA-seq from nuclei sequenced in MOGHE samples, colored by annotated cell type.
741 **(D)** UMAP visualization of snRNA-seq from MOGHE samples integrated with neurotypical WM
742 controls obtained from Elkjaer et al.[29], and colored by cell type.
743 **(E)** Dot plot displaying gene expression levels for canonical markers of major cortical brain cell
744 types. The size of each dot represents the proportion of cells expressing the marker, while the color
745 indicates the average expression levels.
746 **(F)** Dot plot displaying gene accessibility levels computed on the basis of chromatin accessibility
747 for the same marker genes shown in (E). The size of each dot represents the proportion of cells
748 expressing the marker, while the color indicates the average gene accessibility.
749 Astro, astrocytes. EN, excitatory neurons. Endo/VLMC, endothelial/vascular and leptomeningeal
750 cells. IN, inhibitory neurons. OL, oligodendrocytes. OPC, oligodendrocyte precursor cells.
751

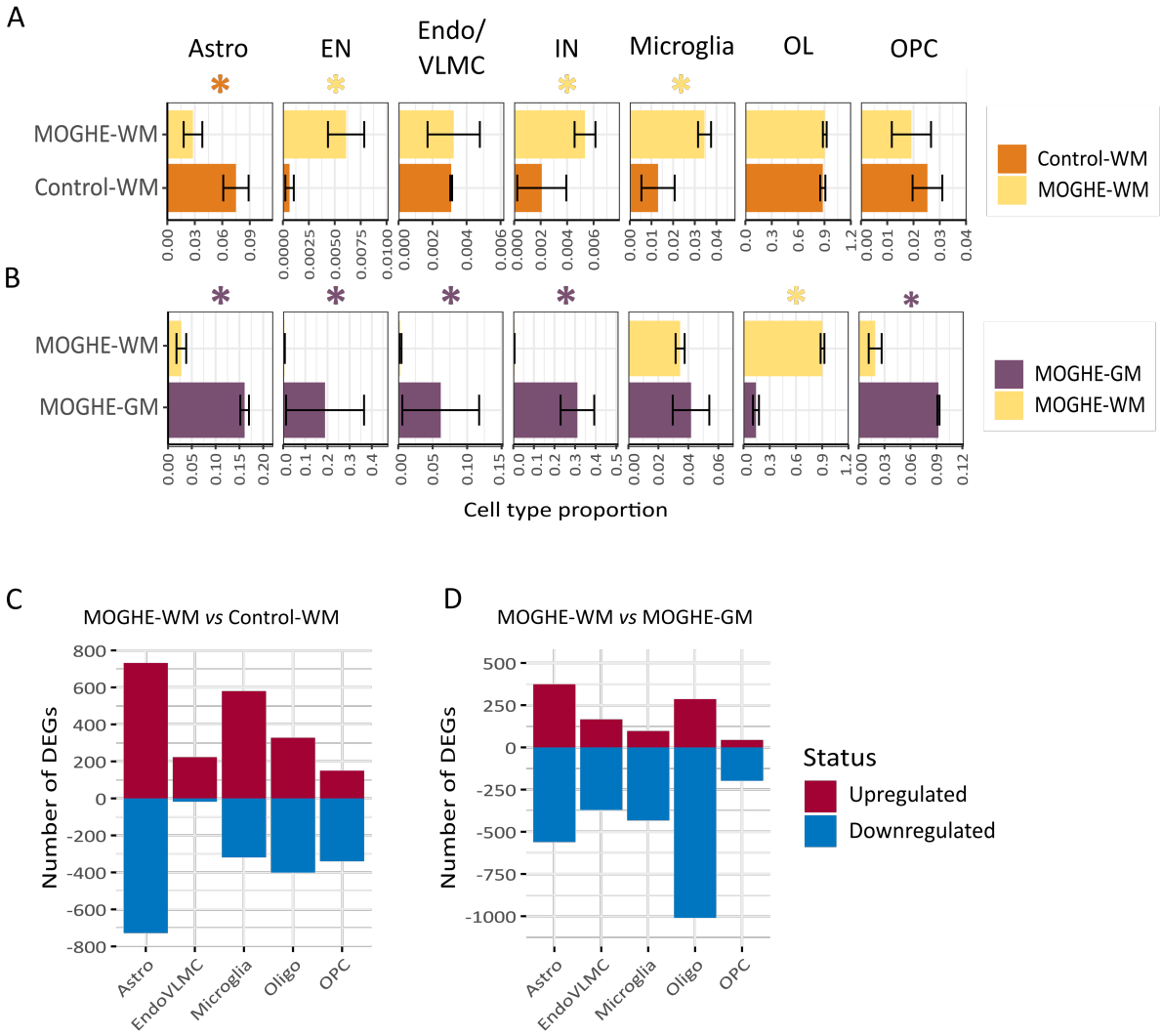

Figure 2. Cell type abundance and gene expression changes in MOGHE.

(A) Barplots denoting cell types abundance in MOGHE-WM and Control-WM samples. The *x*-axis indicates the cell type proportion, and the *y*-axis indicates the tissue type. Error bars indicate the standard error of the mean. Differential cell type abundance was performed using the scProportionTest tool (Methods). Asterisks indicate significant changes considering an FDR < 0.05 and fold-change > 1.5. The asterisk color indicates the tissue type with the higher abundance. (B) Barplots denoting cell types abundance in MOGHE-WM and MOGHE-GM samples. Legends are defined as in (A).

(C) Differentially expressed genes (DEGs) between MOGHE-WM and Control-WM, in non-neuronal populations. DEGs were obtained using MAST, with a fold-change > 2 and adjusted P

value < 0.05. (see Methods). The *x*-axis indicates the cell type, and the *y*-axis indicates the number of DEGs.

(D) DEGs in MOGHE-WM vs MOGHE-GM. Legend is defined in (C).

Astro, astrocytes. EN, excitatory neurons. Endo/VLMC, endothelial/vascular and leptomeningeal cells. IN, inhibitory neurons. OL, oligodendrocytes. OPC, oligodendrocyte precursor cells.

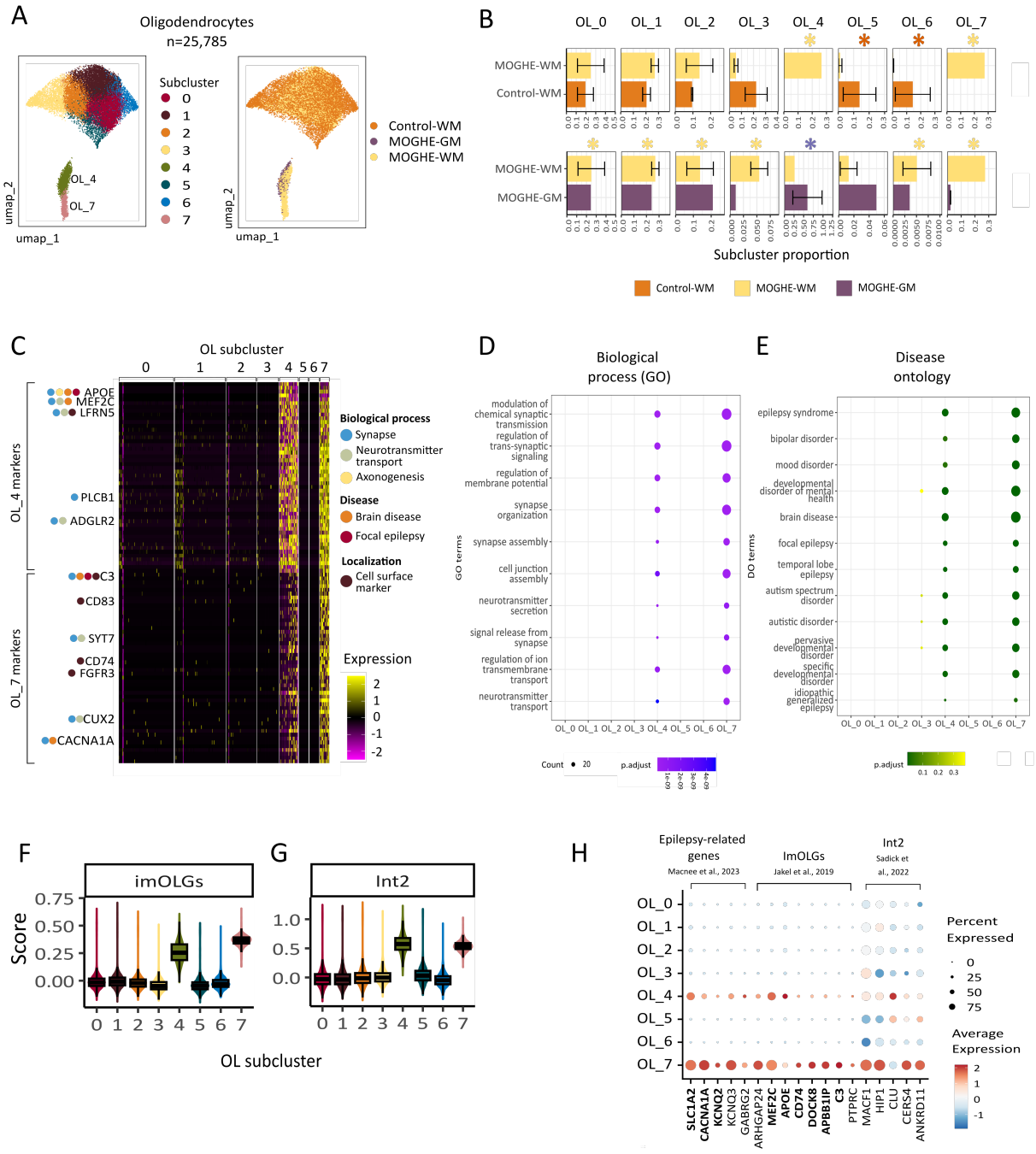

770

771 **Figure 3. Identification of a MOGHE-specific oligodendrocyte population.**

772 **(A)** UMAP representation of oligodendrocytes (OLs) from MOGHE-WM, MOGHE-GM and
773 Control-WM, colored by subcluster (left) and tissue type (right).

774 **(B)** Bar plot showing the OL subcluster proportions in MOGHE-WM and Control-WM samples.
775 The *x*-axis indicates the subcluster proportion, and the *y*-axis indicates the tissue type. Differential
776 subcluster abundance was performed using the scProportionTest tool (Methods). Asterisks indicate
777 significant changes considering an FDR < 0.05 and fold-change > 2. The asterisk color indicates
778 the tissue type with the higher abundance. Error bars indicate standard error of the mean.

779 **(C)** Heatmap showing top marker genes of MOGHE-specific OL_4 and OL_7 subclusters.
780 Biological functions or disease association of selected markers are indicated. The complete list of
781 markers is provided in Supplemental Table 1.

782 **(D)** Dot plot showing top enriched Gene Ontology (GO) terms in OL subclusters computed using
783 clusterProfiler[26]. The size of each dot represents the number of genes associated with the GO term,
784 while the color reflects the enrichment P-value.

785 **(E)** Dot plot showing top enriched Disease Ontology (DO) terms in OL subclusters computed
786 using DOSE[27] and clusterProfiler[26]. The size of each dot represents the number of genes associated
787 with the DO term, while the color reflects the enrichment P-value.

788 **(F)** Boxplots depicting activity scores of the immune oligodendroglia (ImOLG) signature from
789 Jakel et al[33] in OL subclusters. The *x*-axis indicates the subcluster, and the *y*-axis indicates the
790 activity score. The center line of the boxplot shows the median of the data; the box limits show the
791 upper and lower quartiles; the whiskers show 1.5 times interquartile ranges. Overlay dots represent
792 activity scores in individual nuclei.

793 **(G)** Boxplots depicting activity scores of the Int2 OL signature from Sadick et al[34] in subclusters.
794 Legends are defined in (H).

795 **(H)** Dot plot displaying expression levels of gene sets overexpressed in OL_4 and OL_7: epilepsy-
796 associated genes from Macnee et al.[38], genes from the ImOLG signature from Jakel et al.[33], genes
797 from the Int2 signature from Sadick et al.[34], and disease-associated oligodendrocytes (DAOs) from
798 Pandey et al.[64]. The size of each dot represents the proportion of cells expressing the gene in
799 subclusters, while the color indicates the normalized expression level.

800

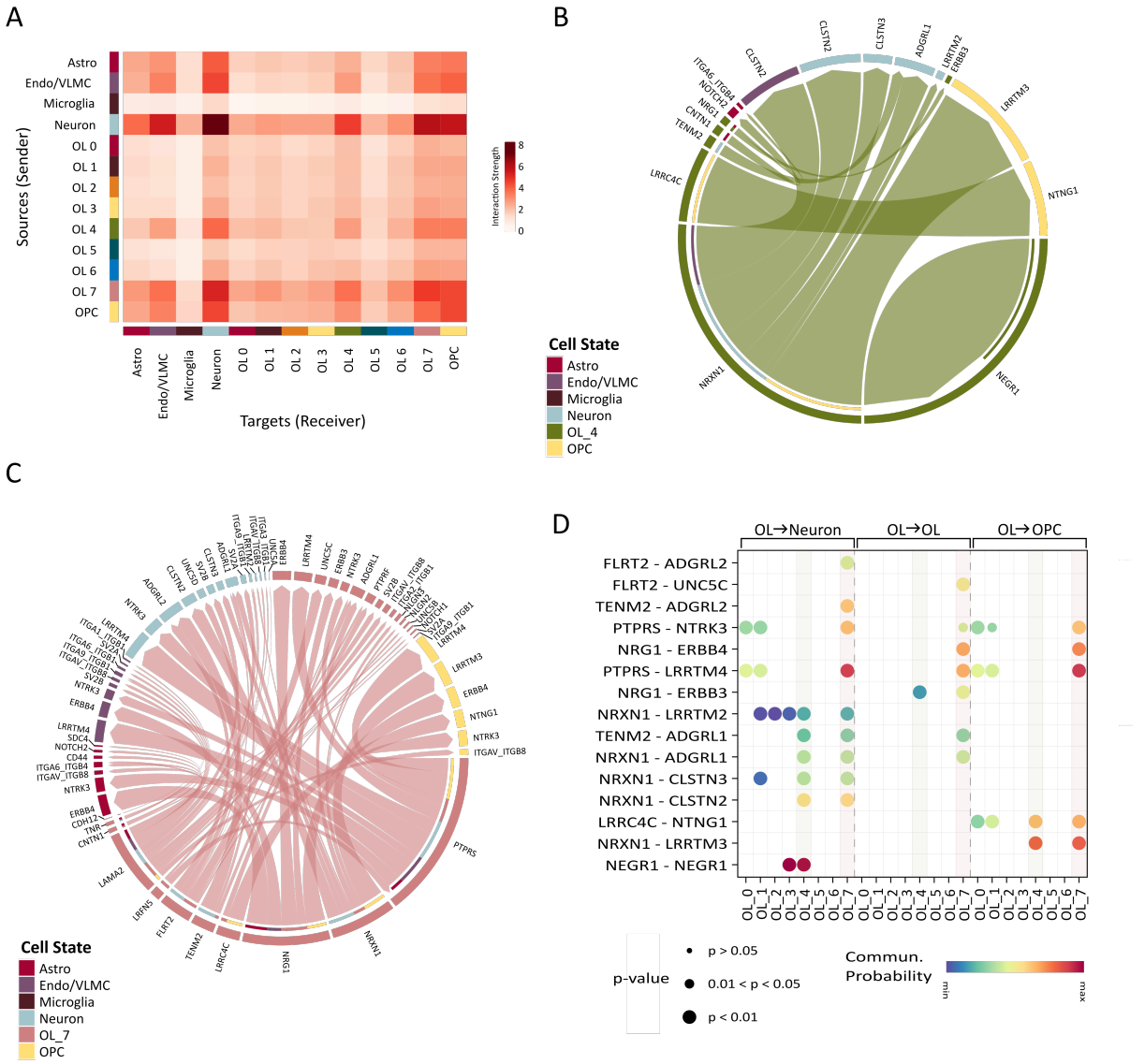

Figure 4. Cell communication analysis of oligodendrocytes (OLs) subclusters.

(A) Heatmap showing interactions across cell types and OLs subclusters inferred by CellChat. The *y*-axis indicates the sources (senders) of the interaction, and the *x*-axis indicates the targets (receivers) of the interaction. Color denotes the interaction strength.

(B) Chord diagram of upregulated ligand-receptor pairs in OL_4 compared to remaining OLs. Colors indicate cell states. Chords are drawn from ligands to receptors and the chord width is proportional to interaction strength. Inner color bars indicate the targets of the corresponding outer color bar. Significant interactions were computed based on percent of cells expressing the ligand > 0.1, p-value < 0.05, and ligand fold-change > 1.5.

811 **(C)** Chord diagram of upregulated ligand-receptor pairs in OL_7 vs remaining OLs. Legends are
812 defined in (B).
813 **(D)** Dot plot of 15 top ligand-receptor pairs upregulated in OL 4 and OL 7 with highest
814 communication probability. The *x*-axis indicates the OL subcluster, and the *y*-axis indicates the
815 ligand-receptor pairs. Dot size indicates the p-value, and dot color indicates the interaction
816 strength. Interactions are shown with OL as sources and either neurons (left), OLs (middle), or
817 OPCs (right) as targets. Light gray vertical bars highlight OL_4 and OL_7 interactions.
818

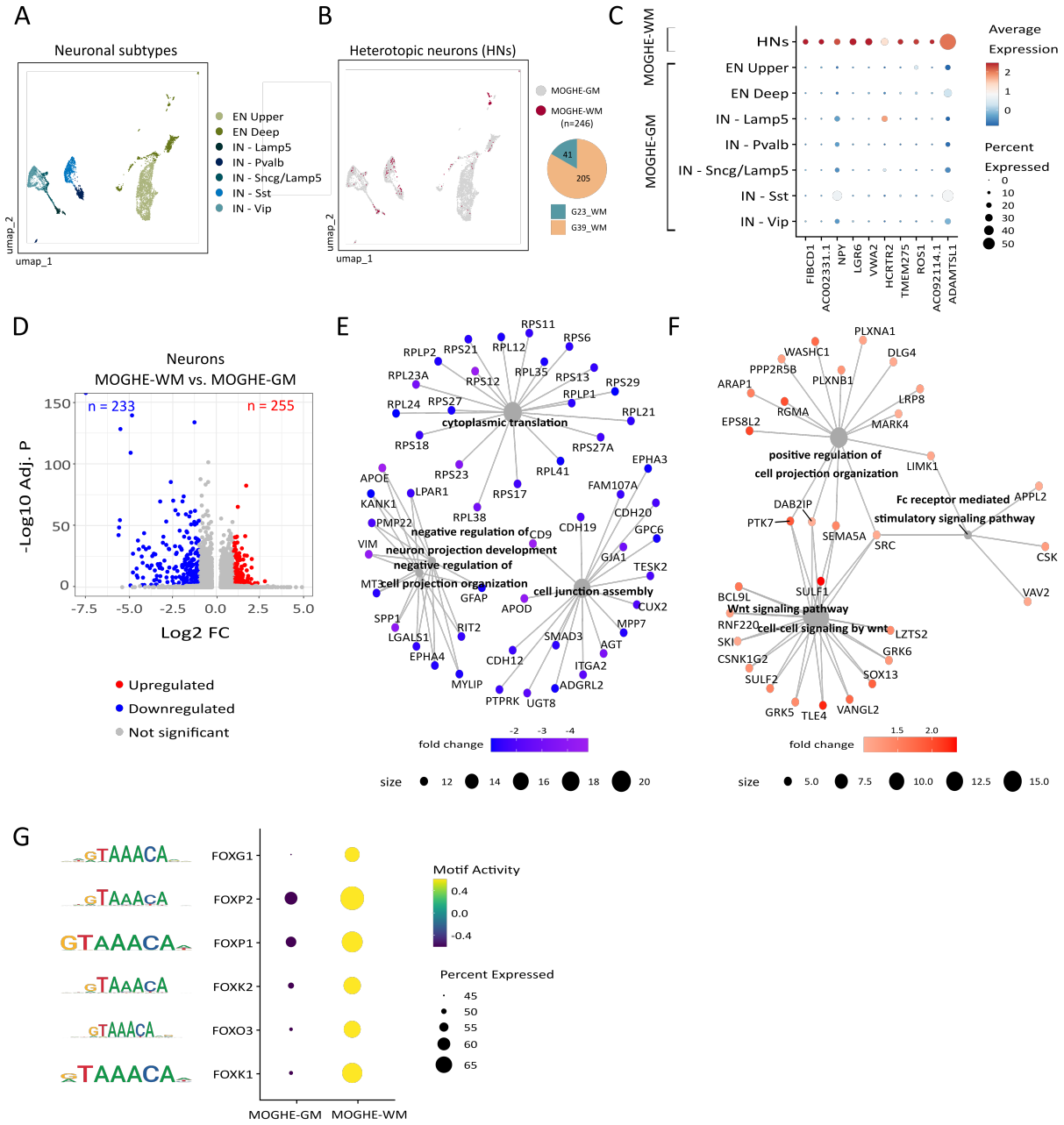

Figure 5. Characterization of heterotopic neurons in MOGHE.

(A) UMAP representation of neuronal nuclei from MOGHE-WM and MOGHE-GM, colored by neuronal subtype.

(B) UMAP representation of neuronal nuclei from (A), colored by tissue origin. Heterotopic neurons (HNs) are indicated in red.

(C) Dot plot displaying gene expression of HNs marker genes. The size of each dot represents the proportion of cells expressing the marker, while the color indicates the average expression levels.

827 **(D)** Volcano plot displaying differentially expressed genes (DEGs) in MOGHE-WM *vs* MOGHE-
828 GM. DEGs were obtained using MAST, with a fold-change > 2 and adjusted P value < 0.05. (see
829 Methods). The *x*-axis indicates the log2 fold-, and the *y*-axis depicts the significance of the change
830 (-log10 of the adjusted P-value). The color indicates the gene status. The complete list of DEGs is
831 available on Supplemental Table 3.
832 **(E)** Gene-term network depicting downregulated genes and corresponding Gene Ontology (GO)
833 molecular functions. GO terms are represented as grey nodes, with size corresponding to the
834 number of associated genes. Genes are colored according to the fold-change values. Enriched GO
835 terms were computed with clusterProfiler.
836 **(F)** Gene-term network illustrating upregulated genes and corresponding molecular functions.
837 Legends are defined in (E).
838 **(G)** Dot plots depicting motif activity of FOX transcription factors in MOGHE-GM and MOGHE-
839 WM neurons. Motif activity was computed using chromVar based on the snATAC-seq datasets.
840 Dot color corresponds to motif activity, and the size corresponds to the proportion of nuclei with
841 open chromatin peaks containing a binding site for the motif. The motif sequence recognized by
842 the regulator is indicated in the left.
843
844
845 **SUPPLEMENTARY FIGURES**
846

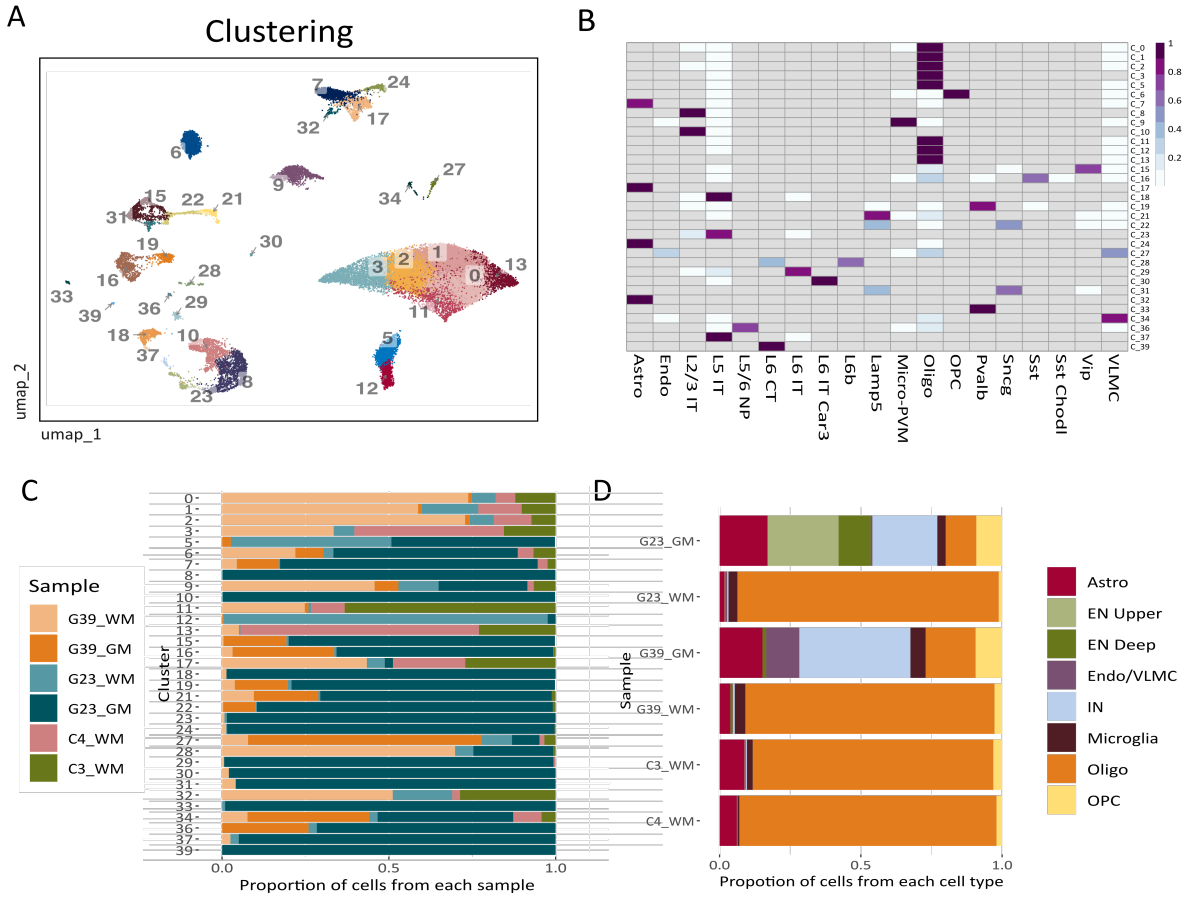

Figure S1, related to Figure 1. Clustering and annotation.

(A) UMAP visualization of nuclei clusters. Clustering was performed in the RNA graph obtained after Harmony integration of MOGHE-WM, MOGHE-GM and Control-WM snRNA-seq samples.

(B) Heatmap depicting the annotation of 40 nuclei clusters performed by Azimuth based on the Allen atlas of the human cortex as a reference. The color indicates the proportion of Azimuth subtypes identified in each cluster.

(C) Bar graphs denoting the representation of samples across nuclei clusters.

(D) Bar graphs showing the proportion of cell types across samples.

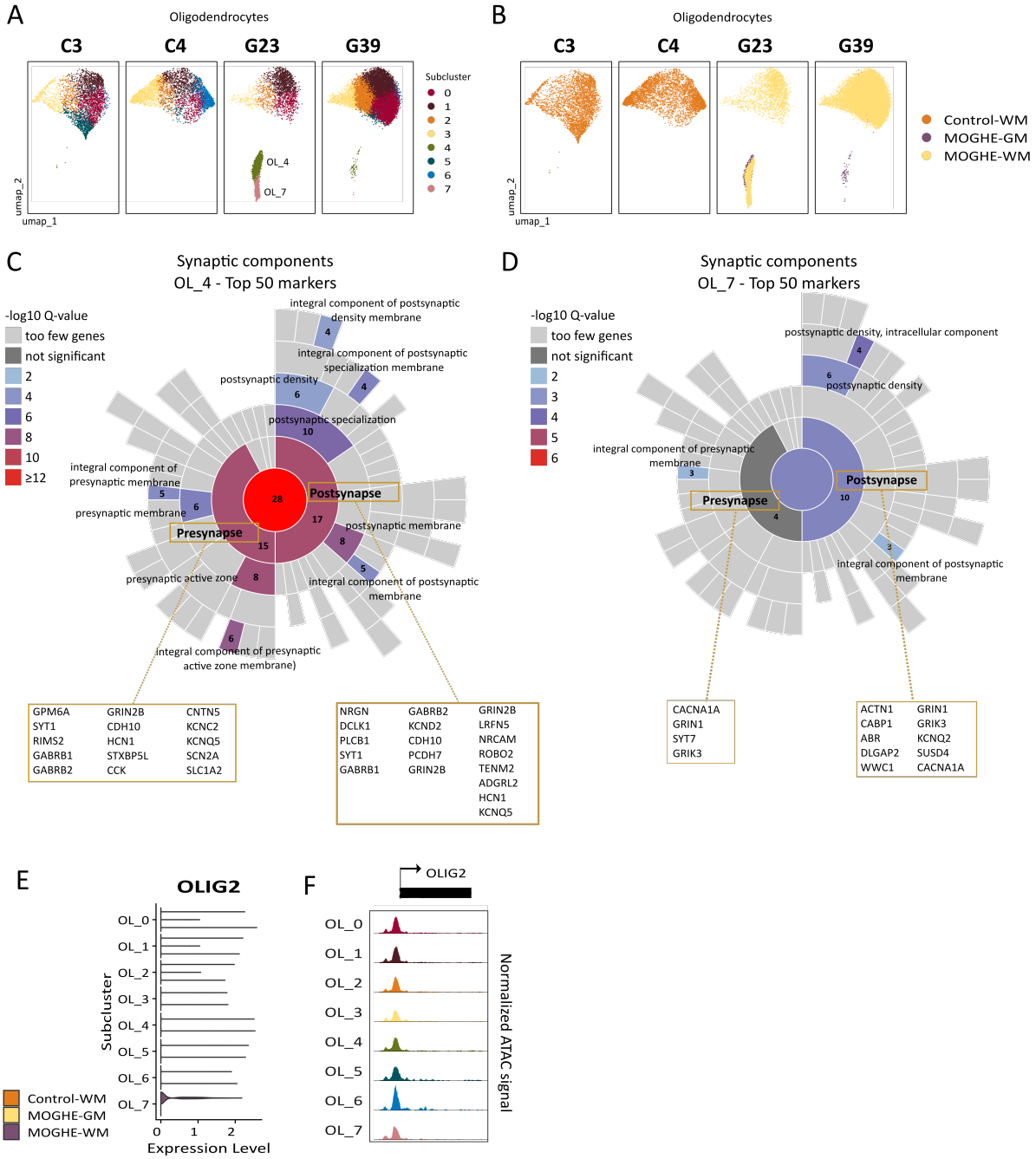

Figure S2, related to Figure 3. Additional information related to MOGHE-specific oligodendrocytes.

(A) UMAP visualization of oligodendrocytes (OLs) in individual MOGHE samples (G23 and G29) and controls (C3, C4), colored by subcluster.

(B) UMAP visualization of OLs in individual MOGHE samples and controls colored by tissue type.

869
870 **(C)** Synaptic Gene Ontology (SynGO) term enrichment analysis based on the top 50 markers genes
871 of the OL_4 subcluster. In the sunburst plot, terms are colored according to their Q-value, and the
872 number of genes corresponding to each synaptic GO term is indicated.
873
874 **(D)** SynGO term enrichment analysis based on the top 50 markers genes of the OL_7 subcluster.
875 Legend is defined as in (C).
876
877 **(D)** Violin plot of *OLIG2* expression in OL subclusters. The *x*-axis indicates the subcluster and the
878 *y*-axis indicates the normalized expression level.
879
880 **(E)** Chromatin accessibility profile of *OLIG2* in OL subclusters from snATAC-seq. The
881 normalized ATAC signal is depicted in a region of +/− 1 kb around the gene start/end coordinates.
882
883
884
885 **SUPPLEMENTARY TABLES**
886
887 **Supplemental Table 1.** Subcluster markers and Gene Ontology (GO)/Disease Ontology (DO)
888 term enrichment analysis associated with OL_4 and OL_7 oligodendrocyte subclusters, related to
889 Fig. 3.
890
891 **Supplemental Table 2.** Synaptic Gene Ontology (SynGO) term enrichment analysis based on the
892 top 50 markers genes of OL_4 and OL_7 subclusters, related to Fig. S2.
893
894 **Supplemental Table 3.** Information related to heterotopic neurons including gene markers,
895 differentially expressed genes, and enriched gene ontology terms, related to Fig. 5.
896
897
898
899